

PCCP

Accepted Manuscript



This is an *Accepted Manuscript*, which has been through the Royal Society of Chemistry peer review process and has been accepted for publication.

Accepted Manuscripts are published online shortly after acceptance, before technical editing, formatting and proof reading. Using this free service, authors can make their results available to the community, in citable form, before we publish the edited article. We will replace this *Accepted Manuscript* with the edited and formatted *Advance Article* as soon as it is available.

You can find more information about *Accepted Manuscripts* in the [Information for Authors](#).

Please note that technical editing may introduce minor changes to the text and/or graphics, which may alter content. The journal's standard [Terms & Conditions](#) and the [Ethical guidelines](#) still apply. In no event shall the Royal Society of Chemistry be held responsible for any errors or omissions in this *Accepted Manuscript* or any consequences arising from the use of any information it contains.

Graphene mechanics: II. Atomic stress distribution during indentation until rupture[†]

Bogdan I. Costescu,^a and Frauke Gräter^{ab*}

Received Xth XXXXXXXXXXXX 20XX, Accepted Xth XXXXXXXXXXXX 20XX

First published on the web Xth XXXXXXXXXXXX 200X

DOI: 10.1039/b000000x

Previous Atomic Force Microscopy (AFM) experiments found single layers of defect-free graphene to rupture at unexpectedly high loads in the micronewton range. Using Molecular Dynamics simulations, we modeled an AFM spherical tip pressing on a circular graphene sheet and studied the stress distribution during the indentation process until rupture. We found the graphene rupture force to have no dependency on the sheet size and a very weak dependency on the indenter velocity, allowing a direct comparison to experiment. The deformation showed a non-linear elastic behavior, with a two-dimensional elastic modulus in good agreement to previous experimental and computational studies. In line with theoretical predictions for linearly elastic sheets, rupture forces of non-linearly elastic graphene are proportional to the tip radius. However, as a deviation from the theory, the atomic stress concentrates under the indenter tip more strongly than predicted and causes a high probability of bond breaking only in this area. In turn, stress levels decrease rapidly towards the edge of the sheet, most of which thus only serves the role of mechanical support for the region under the indenter. As a consequence, the high ratio between graphene sheet and sphere radii, hitherto supposed to be necessary for reliable deformation and rupture studies, could be reduced to a factor of only 5-10 without affecting the outcome. Our study suggests time-resolved analysis of forces at atomic level as a valuable tool to predict and interpret the nano-scale response of stressed materials beyond graphene.

1 Introduction

High mechanical resistance is one of the many intriguing properties of graphene. Recently, Lee *et al.*¹ found graphene to be able to withstand forces up to 2890 nN upon out-of-plane deformation. They used an Atomic Force Microscope (AFM) indenter with a circular tip to obtain load-indentation curves and determine the rupture force for defect-free graphene sheets. Remarkably, due to the extraordinary strength of graphene, they had to resort to diamond tips. They observed a non-linear elastic behavior of the graphene sheet and derived elastic moduli, most importantly a two-dimensional elastic modulus E^{2D} of 342 (± 30) N m⁻¹. The question then arises as to how the single layer of carbon atoms can withstand the enormous out-of-plane forces probed experimentally.

AFM experiments^{1,2} have been used in several studies to develop or parametrize theoretical models using Finite Elements (FE)³ or Molecular Dynamics (MD)⁴ methods. How-

ever, while the experiments were performed with a discrete size AFM indenter tip, these models assumed a point⁴ or cylindrical^{5,6} load, or a vertical load on nanoribbons⁷, and therefore could not take into account the influence of the spherical indenter on the circular plate. Furthermore, they studied only the deformation of the graphene sheet and did not consider the behavior at rupture. Recently, studies investigated graphene indentation and partly also rupture under spherical load in MD simulations^{8,9}, and were able to recover graphene's non-linear elasticity. Other theoretical studies in turn have focused on the mechanical rupture of graphene due to in-plane deformations^{10,11}. However, we are not aware of a study that comprehensively explores graphene indentation and rupture at experimental scales, taking into account the influence of graphene and indenter sizes and indentation velocities. More importantly, the stress distribution within graphene underlying mechanical deformation of this sort has remained elusive. Yet, this internal stress distribution provides the link between the non-linear elastic deformation of graphene under the indenter and the breaking of individual bonds.

The present work attempts to fill in this void by providing an atomic-detail view of time-resolved stresses during graphene deformation and rupture. We perform MD simulations closely mimicking the experiment, allowing us to directly compare the results. The indenter is modeled as a sphere built from discrete atoms; we use a first principles based Morse poten-

[†] Electronic Supplementary Information (ESI) available. See DOI: 10.1039/b000000x/

^a Heidelberg Institute for Theoretical Studies, Schloss-Wolfsbrunnengasse 35, 69118 Heidelberg, Germany

^b CAS-MPG Partner Institute and Key Laboratory for Computational Biology, Shanghai Institutes for Biological Sciences, Chinese Academy of Sciences, 320 Yueyang Road, Shanghai 200031, China

*E-mail: frauke.graeter@h-its.org

tial as presented in Part I¹² and, for a small set of simulations, the AIREBO potential¹³ to allow C-C bond breaking in graphene. All molecular systems are simulated at 300 K, unlike most other studies, which only slightly displaced C atoms from their equilibrium positions to add kinetic energy^{11,14–16}. We first validate our model by comparing the rupture forces for a range of indenter velocities, graphene sheet radii, and indenter radii to the experimental values. For further validation, we compute a two-dimensional elastic modulus from force-indentation profiles obtained from MD simulations, in satisfying agreement with experiments¹. We then study the stress variation in the graphene sheet during the indentation process and before rupture by means of the Time-Resolved Force Distribution Analysis¹⁷ and virial atomic stress calculations. We find a stress concentration at the tip center significantly larger than theoretically predicted, and the probability of bond breaking, and thus of material rupture, to exponentially depend on the tensile force in individual bonds.

2 Methods

We employed MD simulations to study the deformation of finite graphene sheets of circular shape under spherical AFM indenters in vacuum, during which we recorded load-displacement profiles. The calculations were performed with GROMACS¹⁸ 4.5.3 using the truncated Morse potential¹² and LAMMPS¹⁹ version 17Feb2012 using the AIREBO potential¹³. We noticed that the energy conservation was not maintained when the GROMACS calculations were performed in single precision for the larger graphene sheets. Switching to double precision restored the energy conservation, but made the calculations slower. For consistency, we ran all GROMACS calculations in double precision, including those for smaller molecular systems.

The AFM indenter was simulated as a hollow sphere generated from Argon atoms held together by pairwise harmonic potentials. The sphere was constructed from planar circular slices of different diameters, spaced 0.14 nm between them. Each slice is formed by atoms placed at 0.14 nm from each other; only the distance between the first and last atom in the order of placement in one circle is different, to account for the different circle diameters. We found that a single-walled sphere is not able to sustain in some cases the mechanical stress to which it is exposed, leading to deformation and inaccurate load-displacement profiles. Therefore, the spheres used in all simulations were double-walled, the inner wall being generated as another sphere with the radius reduced by 0.14 nm. Pairwise harmonic potentials held together any two Ar atoms located within a distance of 0.25 nm from each other. This distance is smaller than double the initial distance between Ar atoms, such that harmonic potentials only exist between an atom and its direct neighbors from the same

wall or from a different wall. The harmonic potentials have an equilibrium distance of 0.14 nm and a force constant of $7 \cdot 10^6$ kJ mol⁻¹ nm⁻². The force constant was chosen about one order of magnitude larger than any similar value in the OPLS-AA force field²⁰, and a further increase resulted in instabilities of the MD simulations.

Each planar graphene sheet was generated such that the distance between bonded atoms was equal to the C-C equilibrium bond length (0.14 nm). The carbon atoms located at the edge approximated a circle, and were saturated with hydrogen atoms. The graphene sheet and the indenter sphere interacted only through a Lennard-Jones potential. A weak attractive effect of the Lennard-Jones potential was observed at small distances between the sheet and sphere (more details in the ESI[†]).

The largest sheet simulated for this work, with a radius of 100 nm, contained over 1.2 million carbon atoms. Modeling the largest sphere, with a radius of 27.5 nm as in experiments¹, required almost 1 million Ar atoms. Obtaining results for these large systems in reasonable amounts of time was only possible due to the computational simplicity of the truncated Morse potential, due to our approach of using harmonic potentials only between neighboring atoms of the sphere, and due to the high efficiency of the GROMACS code. Still, memory requirements made impossible the simulation of graphene sheets of experimental size (500 nm radius), containing over 30 million atoms.

An energy minimization using the conjugate gradient method was carried out on each molecular system until the maximum atomic force was below 10 kJ mol⁻¹ nm⁻¹. A 1 ns equilibrium MD simulation was then performed starting with random atom velocities generated from a Boltzmann distribution corresponding to a temperature of 300 K; the temperature was maintained at 300 K by separate coupling of the graphene sheet and sphere to velocity rescaling thermostats²¹ with time constants of 100 fs and 20 fs, respectively. The integration time step was 1 fs for GROMACS calculations and 0.5 fs for LAMMPS calculations; the lower value of 0.5 fs is commonly used with the AIREBO potential and increasing it to 1 fs led to instabilities in the MD simulations. No charges were assigned to the atoms. Lennard-Jones interactions were calculated up to a cutoff of 1 nm. For the AIREBO potential, the torsion term was enabled and the Lennard-Jones scale factor was set to 3, leading to a cutoff of 1.02 nm. During the equilibrium MD simulations, ripples formed throughout each graphene sheet due to the thermal motions of the atoms, of amplitude and wave lengths which were in agreement with experiments¹²; the relevance of these ripples during the initial contact of sphere and sheet is detailed in the ESI[†]. From each resulting equilibrium trajectory, we picked the latest frame for which the average position of the C atoms in the Z direction lay within 0.05 nm from the original plane of the graphene sheet, and used it as starting structure for the indentation MD

simulations. To prevent significant deformations of a graphene sheet during these equilibrium simulations due to the ripples, the C atoms at the edge of the sheet were only allowed to move in the XY plane, while the rest of the sheet was allowed to move freely in all three directions.

The equilibrium simulations were followed by constant velocity indentation simulations, with various velocities, as indicated elsewhere in the text, and a force constant of $10000 \text{ kJ mol}^{-1} \text{ nm}^{-2}$. For an indentation velocity of 0.01 nm ps^{-1} , we also performed simulations with a force constant of one order of magnitude smaller and one order of magnitude larger, without observing any significant differences.

During the indentation simulations, C atoms at the edge of the sheet were fixed. This is similar to the experimental setup where it is assumed that the graphene sheet does not slip on top of the rigid support. The sphere was placed above the graphene sheet and the indentation force acted on the center of mass of the sphere, moving it initially towards the sheet and then pressing it onto the sheet. The initial distance between the center of the sphere and the sheet was chosen such that at least 1 ns would pass before the lower side of the sphere touched the graphene sheet. In the AFM experiments, the spherical tip is fixed on the cantilever and pushed vertically into the suspended graphene sheet. To prevent lateral and rotational motion of the sphere in our MD simulations during the out-of-plane indentation along Z, three atoms of the sphere – one located at the top of the sphere and one on each side – were restricted to only move in Z direction. Restricting all sphere atoms to only move vertically would interfere with the temperature coupling, leading to large variations in temperature.

The indentation simulations using the truncated Morse potential were carried out until the first C-C bond broke, which we defined as the initial event of graphene rupture. For the AIREBO potential, the rupture was defined by C atoms moving further than 0.2 nm apart, representing the transition distance between the reactive (REBO) and Lennard-Jones components of the potential.

For each simulation, a finite graphene sheet was placed in an empty simulation box using periodic boundary conditions (PBC), leaving at least 10 nm between the graphene sheet and the box boundaries in the XY plane. In the Z direction, the PBC box was made sufficiently large to fit the initial distance between the sphere and the graphene sheet as well as enough space to allow deformation of the sheet; furthermore, the Z dimension was at least twice as big as the sphere movement in the Z direction. Using a periodic molecular system allowed us to make use of the efficient parallelization scheme based on domain decomposition available in GROMACS 4.0 and later versions. The computation speed was not influenced by the box size as the simulations were performed in vacuum. The LAMMPS simulations did not use PBC, as it does not require periodic boundaries for efficient parallelization.

In all cases, the sphere was allowed to reach the desired constant velocity before touching the graphene sheet; larger spheres contained more atoms and therefore required a higher distance from the sheet in order to reach a constant velocity. Bringing the sphere to a constant velocity of 1 nm ps^{-1} could not be achieved within the maximum distance allowed by the simulation PBC box, setting an upper limit on the indentation velocity. The simulation with the lowest velocity ($0.00003 \text{ nm ps}^{-1}$) took around 21000 hours on modern CPU cores.

We also performed reverse load simulations with a modified version of GROMACS in which the pull code was changed to allow specifying a constant acceleration. The sphere movement had 3 phases: an initial phase in which it moved with constant velocity; a second phase during which a negative acceleration was set, allowing the sphere to slow down, to reach a zero velocity and to start an accelerated movement in the opposite direction; and the final phase in which it again moved with constant velocity.

The calculations of the per atom punctual stress and pairwise forces were performed with the Time-Resolved Force Distribution Analysis (TRFDA) code¹⁷. TRFDA allows efficient monitoring and analysis of forces between pairs of atoms in the molecular system over time. TRFDA defines the per atom punctual stress on atom i as the sum of the scalar values of pairwise forces between atom i and any atom j with which it interacts. For comparison, circular and virial atomic stresses were calculated (for more details see the ESI[†]).

3 Results

Analogous to the AFM indentation experiments of graphene, we performed indentation simulations during which we moved a spherical sphere mimicking the indenter tip at constant velocity into a graphene sheet. We monitored the force as a function of tip indentation until rupture, as shown in Fig. 1a for a graphene sheet with a radius of 25 nm and a tip radius of 5 nm. We recover the highly non-linear elasticity of graphene observed experimentally, with pronounced stiffening during deformation¹. We obtained an average rupture force of $280 (\pm 10) \text{ nN}$ from a series of 100 independent indentation simulations with identical parameters but random starting velocities (Fig. 1a insert). Rupture forces vary among individual trajectories by roughly $\pm 10\%$, again in close agreement with AFM experiments.

We found the indenter velocity of our MD simulations to have only a minor effect on the rupture force. Fig. 1b shows results obtained for a range of simulated velocities covering 4 orders of magnitude. Using a linear regression according to the Bell model^{22,23}, the rupture force estimated for the experimental AFM indenter velocity ($1.3 \cdot 10^{-9} \text{ nm ps}^{-1}$) was less than 4% from the lowest rupture force obtained from MD simula-

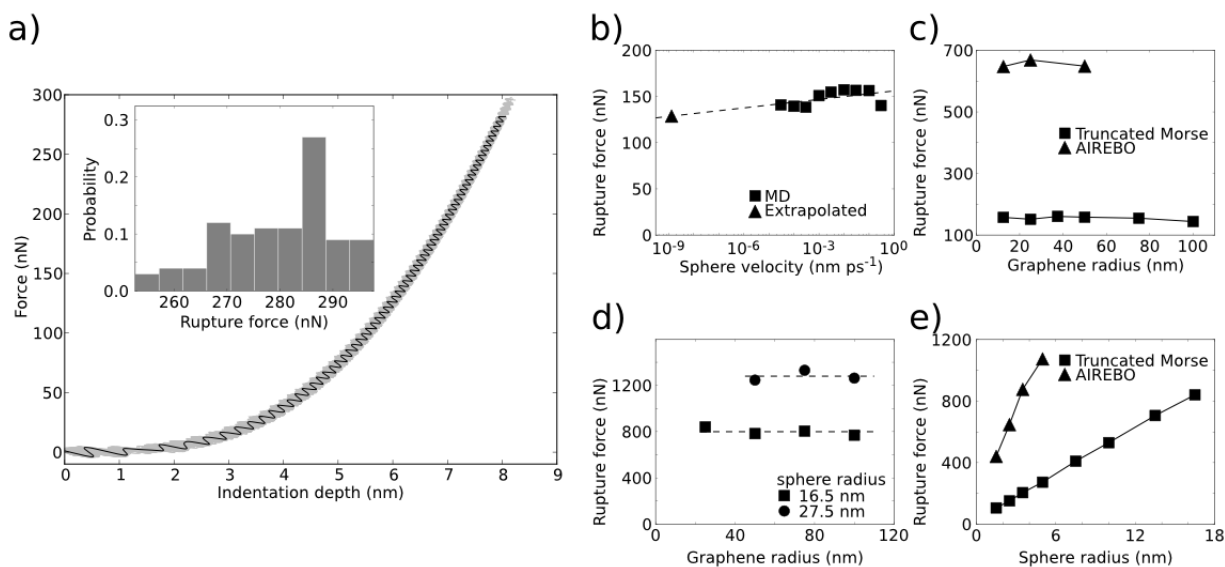


Fig. 1 Variability of rupture force (F_R) and the influence of sphere velocity (v_s), sphere radius (r_s) and graphene sheet radius (r_g). a) Overlay of non-linear force-indentation curves for a set of 100 independent simulations for $r_s=5$ nm and $r_g=25$ nm (gray). One such curve, corresponding to the median rupture force, is shown in black. Inset: histogram of rupture forces with an average of 280 nN. b) Influence of v_s on F_R over four orders of magnitude (squares) for $r_s=2.5$ nm and $r_g=12.5$ nm, using the truncated Morse potential. Lowest F_R is 133 nN corresponding to v_s of 10^{-4} nm ps $^{-1}$. For the experimental v_s of $1.3e-9$ nm ps $^{-1}$ ($=1.3$ μ m s $^{-1}$), the F_R estimated from a linear regression (dashed line) is 129 nN (triangle). c) Influence of r_g on F_R using the truncated Morse potential (squares) and the AIREBO potential (triangles) for $r_s=2.5$ nm and $v_s=0.01$ nm ps $^{-1}$. F_R obtained with the AIREBO potential are 4.2 (± 0.2) times larger than those obtained with the truncated Morse potential. d) Influence of r_s on F_R force using the truncated Morse potential for $r_s=16.5$ nm (squares) and $r_s=27.5$ nm (circles), with $v_s=0.01$ nm ps $^{-1}$. Dashed lines represent average F_R for each sphere radius: for $r_s=16.5$ nm – 800 nN (experimental 1700 nN), for $r_s=27.5$ nm – 1280 nN (experimental 2890 nN). e) Influence of r_s on F_R using the truncated Morse potential for $r_g=25$ nm (squares) and the AIREBO potential for $r_g=12.5$ nm radius (triangles), with $v_s=0.01$ nm ps $^{-1}$. F_R obtained with the AIREBO potential are consistently around 4.2 times larger than those obtained with the truncated Morse potential.

tions, well within the variability range obtained above. Furthermore, a reverse load simulation with a sphere velocity of 0.01 nm ps $^{-1}$ (Fig. S1 in the ESI †) showed that the molecular system is close to equilibrium throughout the indentation process prior to rupture. We conclude that the force-indentation data and rupture forces from our MD simulations can be directly compared to the experimental ones, in spite of a difference of several orders of magnitude in indenter velocity. We used a sphere velocity of 0.01 nm ps $^{-1}$ for all further simulations.

Lee *et al.*¹ suggested that the rupture force does not depend on the graphene sheet radius. We confirmed this finding for a wide range of graphene radii (12.5–100 nm) with both the truncated Morse and the AIREBO potentials (Fig. 1c). Thus, we could use for comparisons spheres with the same radii as the experimental AFM indenters (16.5 and 27.5 nm) but graphene sheets smaller than the experimental ones (20–100 nm instead of 1–1.5 μ m, Fig. 1d). We find the Morse and AIREBO potentials to systematically underestimate or overestimate the experimental rupture force, respectively. More

specifically, the graphene rupture forces obtained with the truncated Morse potential were consistently around 2.2 times smaller than the experimental values and around 4.2 times smaller than the ones obtained with the AIREBO potential (Figs. 1c and 1e). Hence, in spite of ignoring multi-body interactions, the truncated Morse potential predicts a graphene mechanical resistance of the correct order of magnitude as successfully as AIREBO, a more sophisticated and computationally demanding potential. We note that the truncated Morse potential is a pairwise potential developed solely by fitting of the potential energy to quantum mechanical calculations without including any macroscopic material parameters.

Lee *et al.*¹ suggested that the graphene rupture force depends on the AFM indenter radius, with larger tips yielding higher rupture forces. While the experimental data was restricted to only two AFM indenter radii, we could model a much wider range, from 1.5 to 27.5 nm. For both the truncated Morse potential and the AIREBO potential, we observed a perfectly linear dependency of the rupture force on the sphere radius (Fig. 1e). This result is in excellent agreement with the

theoretical predictions of Bathia and Nachbar²⁴ of a spherical indenter pressing on a circular linearly-elastic plate. We conclude that this linear relationship between indenter radius and rupture force might also hold for the more general case of materials with non-linear elasticity like graphene.

Analogous to the procedure by Lee *et al.*¹, we next computed the two-dimensional elastic modulus (E^{2D}) of graphene from the load-indentation data obtained from our MD simulations. Comparing E^{2D} directly to the experimental data and other theoretical models of graphene²⁻⁴ is common practice and avoids defining the thickness of the graphene sheet, which is still controversial²⁵. Fig. 2 shows computed E^{2D} values for varying graphene sheet and tip sizes. Most of the values coming from the simulations using the truncated Morse potential lie within the E^{2D} range derived from experimental data, thus validating once more our model. In contrast, the values coming from simulations using the AIREBO potential were more than 10% smaller than the lower limit of the experimental E^{2D} range. We emphasize that the variability of E^{2D} both in the experiments¹ and in our simulations (with varying graphene and tip size, Fig. 2) is relatively large, so that we refrain from computing and comparing single values of the Young's modulus. Previous studies have attempted to directly match values between MD simulations and AFM experiments and to pinpoint individual sources of errors, overlooking this large variability^{3,6-8,25}, even more so when diverging from experimental conditions. For each sphere radius, E^{2D} obtained with our potential decreased with increasing graphene sheet radius; we hypothesize that this is a result of a too low ratio between the graphene sheet radius and the sphere radius, unlike in the experiments. Indeed, the E^{2D} values apparently converge as the radius of the graphene sheet increases, with spheres of relatively small radii showing a faster convergence with graphene sheet size than the large spheres. Interestingly, towards small graphene sheet sizes, the two potentials show opposite trends for E^{2D} , possibly because of the heterogeneity in bond orders allowed by the AIREBO potential.

Having validated our computational model, we next aimed at explaining the material failure and its dependence on sheet and tip size by monitoring the internal stress distribution of graphene under mechanical load. To this end, using Time-Resolved Force Distribution Analysis¹⁷, we calculated a per atom punctual stress on each atom i , which is defined as the sum of scalar forces between pairs of atoms i and j and therefore expressed in units of force. We also carried out similar calculations for virial atomic stress²⁶ and a circular stress defined as the sum of pairwise forces acting across circles concentric with the graphene sheet. Normalization of these three alternative definitions of stress by the area of action of pairwise atomic forces, atomic volume or height of the single atom thick layer, respectively, would yield true stresses, however these quantities are ill-defined (more details on stress calcu-

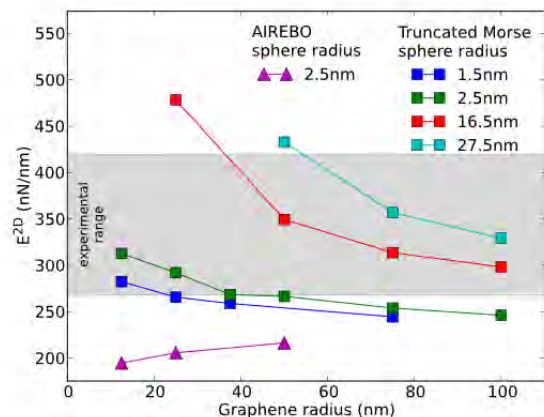


Fig. 2 Two-dimensional elastic modulus (E^{2D}) for various sphere radii and graphene sheet radii, using the truncated Morse (squares) and AIREBO (triangles) potentials. The horizontal gray area shows the range of E^{2D} values obtained from experiments by Lee *et al.*¹.

lations can be found in the ESI[†]). The following findings on stress distribution in indented graphene hold for any of the three different stress definitions, and we focus below on the results for the per atom punctual stress.

Fig. 3a shows a typical stress distribution in the graphene sheet during the indentation process; a dynamical representation, with atoms colored by stress, can be seen in Movies M1 and M2 in the ESI[†]. At the start of the indentation process, while the sphere is some distance away, spontaneous ripples, which form throughout the graphene sheet due to thermal fluctuations at room temperature^{12,27,28}, give rise to a low level of background stress. During the indentation process, the stress increases significantly only in and around the area of graphene in contact with the sphere, and remains at levels comparable to the background stress towards the edge of the sheet, even for small ratios between the graphene sheet and sphere radii. The stress distributions during the indentation process for the circular stress and virial atomic stress are very similar, as can be seen in the ESI[†] (Fig. S2).

How does the stress distribution depend on the graphene and sphere size, in comparison to the dependence of the graphene rupture force on these geometrical parameters? Interestingly, the radial stress at a certain distance from the sheet center, measured shortly before graphene rupture, does not depend on the sheet radius, even for sheet sizes (down to 3 nm) approaching the sphere size (2.5 nm, Fig. 3b). Similarly, the contact area between the sphere and the sheet is independent of the sheet size (Fig. S3 in the ESI[†]). We observe a highly localized stress concentration under the sphere, with the stress near the edge of the sheet already reaching background levels for a ratio of sheet to sphere radius of 5–10 (Fig. 3c; Fig.

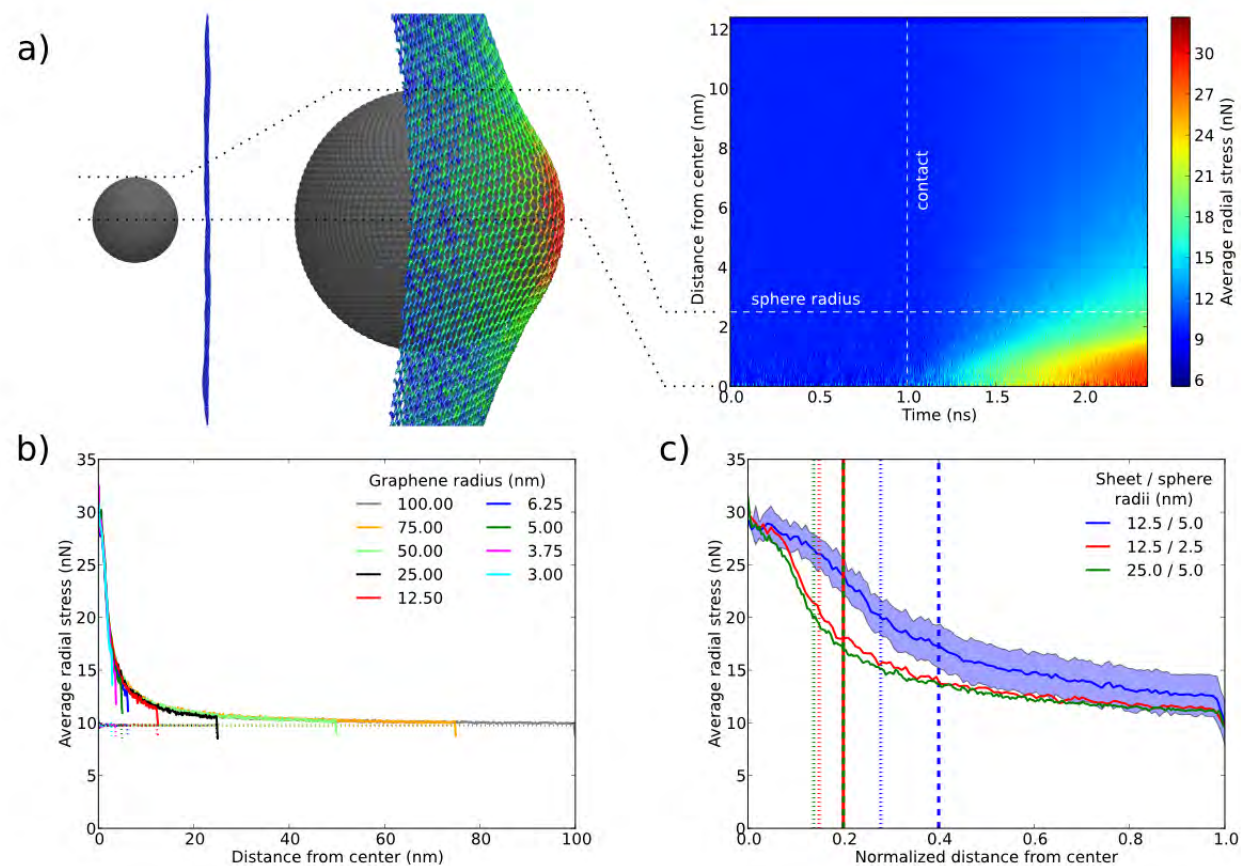


Fig. 3 Stress variation during indentation and just before rupture, for a sphere velocity of 0.01 nm ps^{-1} . The averaged radial stress was obtained by averaging the per atom punctual stress over all atoms found at the same distance from the center of the graphene sheet. The distance from the center was computed with a resolution of 0.1 nm . a) Variation of averaged radial stress as a function of distance from the center of the graphene sheet and time for a sphere radius $r_s=2.5 \text{ nm}$, a graphene sheet radius $r_g=12.5 \text{ nm}$. The left snapshot shows the background stress before the indentation in a side view of the whole molecular system. The right snapshot shows the distribution of per atom punctual stress, 1 ps before the rupture, in a detailed side view. b) Averaged radial stress less than 100 ps before rupture as a function of distance from the center of the sheet for $r_s=2.5 \text{ nm}$ and several r_g . Dotted lines show the background stress. c) Averaged radial stress less than 100 ps before rupture for several r_g/r_s pairs: $12.5/2.5$ (red), $12.5/5.0$ (blue) and $25.0/5.0$ (green), as a function of distance from the center normalized by r_g . The shaded area shows the standard deviation for one of the curves. Dashed lines show r_s , dotted lines show the radii of the contact area between the sheet and the sphere.

S4 and S5 in the ESI[†]), while the theoretical model assumes this ratio to be much larger^{1,24}. Similarly, we obtain ratios of $1.4\text{--}1.9$ between the stress at the center of the sheet and the stress at the edge of the contact area between sphere and sheet (dotted lines in Fig. 3c), a range which is significantly larger than 1.17 suggested in the analytical model²⁴. Taken together, this suggests that a small area under and around the sphere, determined only by the sphere radius, is sufficient to bear the load, while the rest of the sheet only serves the role of mechanical support for this central area. This finding offers a straightforward explanation for the previous results from experiments¹ of graphene rupture force being independent from

the sheet radius. Unexpectedly, our simulations suggest that both the stress distribution and the rupture force of the sheet (Fig. 1c) remain consistent all the way down to sheet sizes only marginally larger – by roughly 20% – than the indenter. Thus, we propose that similar AFM experiments could be performed with significantly larger indenters or smaller graphene sheets than previously used, without affecting the outcome. In particular, it might be considerably easier to obtain smaller defect-free graphene sheets for such experiments.

In sharp contrast to the independence with regard to graphene size, the stress distribution is strongly influenced by the sphere radius (Fig. 3c). For a given graphene sheet, en-

larging the sphere radius from 2.5 to 5 nm results in a correspondingly wider stress distribution and contact area. As a result, the center of the graphene sheet reaches the critical radial stress of ~ 30 nN, at which we observe rupture, at an indentation force of ~ 284 nN for a 5 nm sphere, as opposed to ~ 160 nN for a sphere of half the radius. Stress profiles along normalized distances from the center, however, overlap for the same ratio between the graphene sheet radius and the sphere radius (Fig. 3c).

We established above that stress distributions in the whole sheet and rupture forces are qualitatively linked, as they show parallels in their dependency on sphere and sheet size (compare Figs. 1d,e and Figs. 3b,c). We next quantitatively assess this link by investigating how stress in a bond determines its likelihood to break. Fig. 4a shows the breaking probability of a bond as a function of its distance from the center of the graphene sheet, obtained from 100 independent trajectories initiated with different random velocities. Upon graphene indentation by a sphere of 5 nm radius, the probability of a bond to break vanishes quickly as the distance from the center increases. The probabilities become lower than 1% at distances beyond 1.2 nm, *i.e.* still well below the sphere radius, reflecting the high concentration of stresses right under the AFM indenter. In agreement, Lee *et al.*¹ observed graphene rupture to exclusively start at the indentation point. We note that our model of the graphene sheet did not assume a particular bond or bonds in certain regions of the sheet to break, in contrast to previously investigated models based on quantum mechanics or hybrid quantum mechanics/molecular mechanics^{29,30}. Furthermore, we also tested how the local geometry of the network of C-C bonds can influence the results. If an atom is found at the center of the graphene sheet, the load transmitted from the tip of the indenter can stretch the three C-C bonds formed by this atom; if the center of the sheet is found in the middle of an aromatic ring, the load can stretch the six C-C bonds forming the ring. From a small set of simulations comparing these two cases, we obtained results indistinguishable from each other. This is consistent with our previous finding that the first bond which breaks is not always one formed by the central atom. It also agrees very well with the experimental conditions¹ in which the location of the AFM indenter is only precise to within 50 nm from the center of the graphene sheet.

To correlate the likelihood of bond breaking with the tensile stresses induced in bonds by the indentation process, we performed an analysis of the individual C-C bond forces in the graphene sheet. We note that stresses in bonds are equivalent to C-C bond forces, as the sectional area of a bond is not well defined, but can be assumed to be the same for all bonds in the sheet as graphene is a homogeneous material. As shown in Fig. 4b, the forces have a wide distribution but small average values for the outer regions of the sheet, suggesting a low

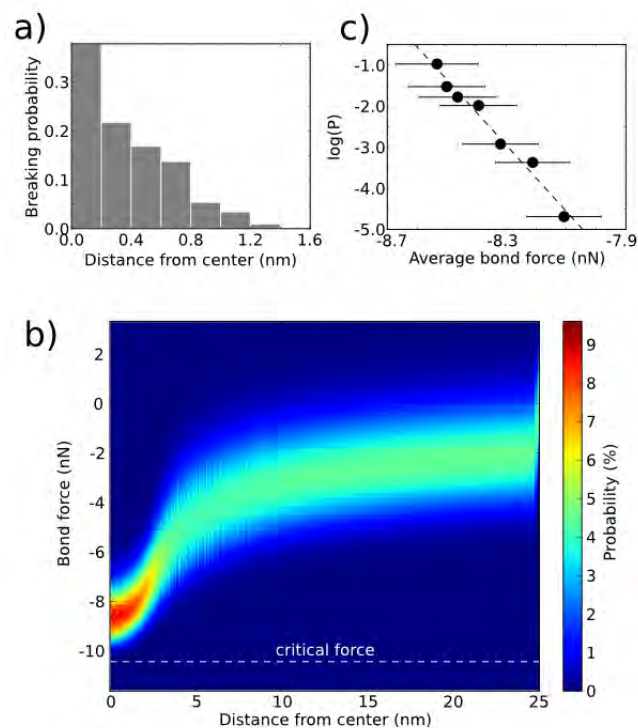


Fig. 4 Bond breaking probability from a series of 100 independent simulations with a sphere radius of 5 nm, a graphene sheet radius of 25 nm and a sphere velocity of 0.01 nm ps^{-1} . The distance was calculated between the center of the sheet and the closest of the two atoms forming the bond which breaks, with a resolution of 0.1 nm. By convention, an attractive force is negative. a) Probability of bond breaking as a function of distance from the center of the graphene sheet. The number of broken bonds in each bin was normalized by the total number of bonds in that bin. b) Distribution of C-C bond forces as a function of distance from the center of the graphene sheet. For each distance from the center, the distribution reflects C-C bond forces from the last 100 ps before the first bond breaking. c) Probability of bond breaking as a function of the bond force. The averages and standard deviations are calculated over data from the 100 independent simulations; each data was the median of the forces in bonds located at the same distance from the center of the sheet for the last 100 ps before the first bond breaking. Error bars indicate the standard deviation. The dashed line represents a Bell model fit with $\Delta x_{\text{bond}} = 0.034 \text{ nm}$ and an average bond force at 100% probability of -8.7 nN .

probability of bond breaking. In contrast, the distribution becomes narrower and the forces are significantly larger towards the center of the sheet, most distinctly at distances smaller than the sphere radius (5 nm) from the center. The higher probability of larger forces implies a higher probability of reaching the critical force for bond breaking. Indeed, Fig. 4c shows an exponential dependency of the probability of bond breaking on

the average tensile force in the bond. Extrapolating to a probability of 100% results in a critical value of 8.7 nN, which is slightly lower than the value of ~ 10.4 nN for C-C bond breaking defined in our force field, suggesting force fluctuations at 300 K (error bars in Fig. 4c) to play a critical role in propagating a tensed bond to a broken state (see also Movie M3 in the ESI[†]).

Considering graphene rupture as a two-state kinetic process, driven by the extension of a single bond from the bonded to the broken state, and regarding the bond length as reaction coordinate, we fitted the Bell model^{22,23} to the data in Fig. 4c (see the ESI[†] for details). We obtained a distance from the reactant to the transition state $\Delta x_{\text{bond}} = 0.034$ nm, which is comparable to the difference between the average bond length (0.142 nm) in equilibrium simulations and the critical bond length (0.184 nm) defined for the truncated Morse potential¹². From a similar Bell model fit to the rupture force dependency on indenter velocity (Fig. 1b), and regarding the direction of indentation as reaction coordinate, we obtained a distance $\Delta x_{\text{indent}} = 1.4 \cdot 10^{-3}$ nm, one order of magnitude smaller than Δx_{bond} . This discrepancy originates in the different orientation of the reaction coordinate; C-C bonds under the indenter tip are nearly perpendicular to the indentation direction, so the projection of their lengthening up to their breaking point results in a Δx_{indent} on the very small sub-Ångström scale. Thus, while the kinetics of individual bond breaking are determined by the energy landscape of the single bonds, graphene sheet rupture is dominated by a projection of that energy landscape along the direction of the sheet indentation.

4 Discussion and conclusions

In MD simulations, we replicated as close as possible the experiments of Lee *et al.*¹ measuring load-indentation profiles and determining the rupture forces for defect-free graphene sheets. This approach allows us to make direct comparisons of the results without relying on approximations, and to further validate the truncated Morse potential used to model the C-C bonds in graphene (see Part I¹²). While previous theoretical work derived elastic parameters from deformation studies^{3,4,25}, we here focus on the material rupture and internal stress distribution as its molecular basis.

Although the truncated Morse potential is a simple pairwise potential, the deformation and rupture results obtained with it are as close to the experimental ones as the results obtained with the AIREBO potential or in some cases (E^{2D}) even closer. While the truncated Morse potential correctly predicts the stiffness but underestimates the strength of graphene, the AIREBO potential predicts a too low stiffness and at the same time a too high strength. Given its better prediction of the mechanical stiffness and due to its relative low computational complexity when compared to AIREBO or other bond order

potentials (see Part I¹²), the truncated Morse potential represents a good choice for further theoretical studies on graphene mechanics, especially in multi-million atom systems.

Our results show that the rupture force depends on the indenter sphere radius and does not depend on the graphene sheet radius, in agreement with experiments. Unlike Lee *et al.*¹ who assumed a large ratio between the graphene sheet and sphere radius, our results suggest that the rupture force remains the same even for a ratio approaching one. Furthermore, our results show that the rupture force depends linearly on the sphere radius, as previously only predicted by an analytical model for a purely elastic material.

Using TRFDA and atomic stress calculations, we were able to study the variation of stress in the graphene sheet during the indentation process until rupture. The stress distribution just before rupture suggests that a small central area of the sheet bears most of the load while the rest of the sheet only acts as a mechanical support for it. The observed stress concentration differs from finite element simulations¹ and analytical models of elastic materials²⁴. Generalizing the available analytical theory to describe the deformation and stresses in a planar material under a spherical indenter²⁴ to non-linearly elastic materials like graphene would be desirable to test our predictions, and interpret previous and future indentation experiments.

Stress calculations in MD simulations are not straightforward. Stress is typically defined in units of force over area, but the area of action of an atomic pairwise force or the sectional area of a single atom thick layer are not well defined. For this reason, TRFDA¹⁷ calculates a per atom punctual stress as the sum of scalar pairwise forces acting on the atom and ignores the area of action of a pairwise force. The virial atomic stress²⁶ uses a different but equivalent expression of energy over volume, in which the volume of an atom is also ill-defined and thus ignored. For the case of a single atom thick layer, a more realistic definition is the circular stress, calculated as the total force acting across a circle of known length in the plane of the layer, though this definition still ignores the thickness of the layer. Graphene is a homogeneous material, and therefore the area of action of the atomic pairwise forces, the volume of an atom and the thickness of the sheet can be considered constant and appear only as normalization factors in stress calculations. Consequently, all three stress definitions should be valid when applied to graphene, even though the absolute values of the stress are expressed in different units and cannot be directly compared. Indeed, our results show an excellent agreement between the stress distributions during indentation until rupture for the three different definitions of stress.

Using our analysis of the tensile forces in strongly indented graphene, we could show that thermal fluctuations in highly tensed bonds under the indenter initiate the rupture of the material. The probability of a bond to break decays rapidly to

wards the outer graphene regions and the decay is determined by the sub-Ångström lengthening of bonds to their critical length. Our analysis can also predict the rupture under load of other materials for which a (possibly truncated) Morse potential is an appropriate model of the interatomic bonds. Considering the same dissociation energy, a broader Morse potential translates into a larger critical bond length but lower critical force. Therefore, thermal fluctuations in the stretched material generate a wider distribution of bond lengths and lead to reaching the critical force earlier. This increases the area around the center of the sheet where the bonds have a high probability of breaking and thus the rupture initiation becomes less localized under the AFM indenter. Conversely, a narrower Morse potential leads to a tighter area around the center of the sheet where the material rupture can start.

Overall, we find graphene rupture to be mostly described by two geometrical coordinates. The macroscopic indentation and stretching of the sheet sets the graphene rupture force sensitivity on the indenter size, while the microscopic bond lengthening sets the locality of the rupture initiation events. It remains to be investigated how defects present in the graphene sheet change the behavior at these two different scales. Few, small defects can potentially lead to a localized broadening of the range of bond forces. If such defects are found in the area of the sheet under the indenter, characterized by a narrow range of high forces, they would increase the probability of reaching the critical force and therefore of rupture. If the defects are found in the outer regions of the sheet, their impact on the already wide range of low bond forces would be minimal. However, numerous or large defects will significantly disturb the network of C-C bonds, such that the stress distribution and rupture probabilities can no longer be inferred from the current results.

5 Acknowledgments

We are grateful to Christian Seifert, Murat Cetinkaya, Sandeep Patil and Camilo Aponte-Santamaria for helpful discussions, and to Jan Hamaekers for pointing us to the AIREBO potential. We thank the Klaus Tschira Foundation for financial support.

References

- C. Lee, X. Wei, J. W. Kysar and J. Hone, *Science*, 2008, **321**, 385–388.
- I. W. Frank, D. M. Tanenbaum, A. M. van der Zande and P. L. McEuen, *Journal of Vacuum Science & Technology B*, 2007, **25**, 2558–2561.
- F. Scarpa, S. Adhikari, A. J. Gil and C. Remillat, *Nanotechnology*, 2010, **21**, 125702.
- W. H. Duan and C. M. Wang, *Nanotechnology*, 2009, **20**, 075702.
- L. Zhou, J. Xue, Y. Wang and G. Cao, *Carbon*, 2013, **63**, 117–124.
- L. Zhou, Y. Wang and G. Cao, *Journal of Physics: Condensed Matter*, 2013, **25**, 475303.
- S. Y. Kim, S.-Y. Cho, J. W. Kang and O. K. Kwon, *Physica E: Low-dimensional Systems and Nanostructures*, 2013, **54**, 118–124.
- X. Tan, J. Wu, K. Zhang, X. Peng, L. Sun and J. Zhong, *Applied Physics Letters*, 2013, **102**, 071908.
- Y.-C. Fan, C.-D. Wu, T.-H. Fang and T.-H. Chen, *Computational Materials Science*, 2013, **79**, 105–109.
- R. Faccio, P. A. Denis, H. Pardo, C. Goyenola and Á. W. Mombrú, *Journal of Physics: Condensed Matter*, 2009, **21**, 285304.
- C. D. Reddy, S. Rajendran and K. M. Liew, *Nanotechnology*, 2006, **17**, 864.
- B. I. Costescu, I. B. Baldus and F. Gräter, *Physical Chemistry, Chemical Physics*, 2014, **99999**, 99999.
- S. Stuart, A. Tutein and J. Harrison, *Journal of Chemical Physics*, 2000, **112**, 6472–6486.
- T. Belytschko, S. P. Xiao, G. C. Schatz and R. S. Ruoff, *Phys. Rev. B*, 2002, **65**, 235430.
- V. B. Shenoy, C. D. Reddy, A. Ramasubramaniam and Y. W. Zhang, *Phys. Rev. Lett.*, 2008, **101**, 245501.
- R. C. Thompson-Flagg, M. J. B. Moura and M. Marder, *EPL (Europhysics Letters)*, 2009, **85**, 46002.
- B. I. Costescu and F. Gräter, *BMC Biophysics*, 2013, **6**, 5.
- B. Hess, C. Kutzner, D. van der Spoel and E. Lindahl, *Journal of Chemical Theory and Computation*, 2008, **4**, 435–447.
- S. Plimpton, *Journal of Computational Physics*, 1995, **117**, 1–19.
- W. L. Jorgensen, D. S. Maxwell and J. Tirado-Rives, *Journal of the American Chemical Society*, 1996, **118**, 11225–11236.
- G. Bussi, D. Donadio and M. Parrinello, *Journal of Chemical Physics*, 2007, **126**, 014101.
- G. Bell, *Science*, 1978, **200**, 618–627.
- E. Evans and K. Ritchie, *Biophys J*, 1997, **72**, 1541–1555.
- N. Bhatia and W. Nachbar, *International Journal of Non-Linear Mechanics*, 1968, **3**, 307–324.
- F. Scarpa, S. Adhikari and A. S. Phani, *Nanotechnology*, 2009, **20**, 065709.
- A. P. Thompson, S. J. Plimpton and W. Mattson, *The Journal of Chemical Physics*, 2009, **131**, 154107.
- N. Abedpour, M. Neek-Amal, R. Asgari, F. Shabbazi, N. Nafari and M. R. R. Tabar, *Phys. Rev. B*, 2007, **76**, 195407.
- A. Fasolino, J. H. Los and M. I. Katsnelson, *Nat Mater*, 2007, **6**, 858–861.
- R. Grantab, V. B. Shenoy and R. S. Ruoff, *Science*, 2010, **330**, 946–948.
- R. Khare, S. L. Mielke, J. T. Paci, S. Zhang, R. Ballarini, G. C. Schatz and T. Belytschko, *Phys. Rev. B*, 2007, **75**, 075412.